

twoPhaseInterTrackFoam: an OpenFOAM module for Arbitrary Lagrangian/Eulerian Interface Tracking with Surfactants and Subgrid-Scale Modeling

Moritz Schwarzmeier^a, Suraj Raju^a, Željko Tuković^b, Mathis Fricke^a, Dieter Bothe^a, Tomislav Marić^{a,*}

^a*Mathematical Modeling and Analysis Institute, Mathematics department, TU Darmstadt, Germany*
^b*Faculty of Mechanical Engineering and Naval Architecture, University of Zagreb, Croatia*

Abstract

We provide an implementation of the unstructured Finite-Volume Arbitrary Lagrangian / Eulerian (ALE) Interface-Tracking method for simulating incompressible, immiscible two-phase flows as an OpenFOAM module. In addition to interface-tracking capabilities that include tracking of two fluid phases, an implementation of a Subgrid-Scale (SGS) modeling framework for increased accuracy when simulating sharp boundary layers is enclosed. The SGS modeling framework simplifies embedding subgrid-scale profiles into the unstructured Finite Volume discretization. Our design of the SGS model library significantly simplifies adding new SGS models and applying SGS modeling to Partial Differential Equations (PDEs) in OpenFOAM.

Keywords:

finite volume, interface tracking, ALE, unstructured mesh, subgrid-scale

PROGRAM SUMMARY

Program Title: twoPhaseInterTrackFoam

CPC Library link to program files: (to be added by Technical Editor)

Developer's repository link: <https://gitlab.com/interface-tracking/twophaseintertrackfoamrelease>

Code Ocean capsule: (to be added by Technical Editor)

Licensing provisions: GPLv3

Programming language: C++

Nature of problem:

Two-phase flow problems involving surface-active agents (surfactants), variable surface tension force and very sharp boundary layers.

Solution method:

An OpenFOAM implementation of the Arbitrary Lagrangian / Eulerian Interface Tracking method.

*Corresponding author

Email addresses: schwarzmeier@mma.tu-darmstadt.de (Moritz Schwarzmeier), raju@mma.tu-darmstadt.de (Suraj Raju), zeljko.tukovic@fsb.unizg.hr (Željko Tuković), fricke@mma.tu-darmstadt.de (Mathis Fricke), bothe@mma.tu-darmstadt.de (Dieter Bothe), maric@mma.tu-darmstadt.de (Tomislav Marić)

1. Introduction

The unstructured Finite Volume Arbitrary Lagrangian / Eulerian Interface Tracking method in OpenFOAM (ALE-IT) [31, 29] is a highly accurate method that tracks fluid phases as deforming solution domains separated by domain boundaries, making it possible to accurate account for jump conditions at moving domain boundaries shared by two fluid phases, as well as to solve Partial Differential Equations (PDEs) on moving domain boundaries. The ALE-IT method has been successfully applied to challenging two-phase flow problems, involving, e.g., two-phase flows with soluble surfactant [9, 10, 22] and two-phase flows with interfacial mass transfer [33, 23].

The Subgrid-Scale (SGS) modeling [1, 4, 34] employs an analytical solution to enhance the computation of passive scalar transport in interfacial boundary layers, saving multiple local refinement levels of Finite Volume mesh. This can accordingly speed up simulations, enable them in the first place or save (computing) resources, while delivering results with high accuracy.

With this publication, we provide an open-source implementation of our ALE-IT method as an OpenFOAM module. The version used to generate results from this manuscript is *v1.0*, available in the GitLab repository [25] and archived as [30]. Results reported in this paper are archived as [26]. The following sections cover the details of the mathematical model, equation discretization, and subgrid-scale modeling implemented in the version *1.0* of our ALE-IT OpenFOAM module, as well as the results for some showcases.

2. Mathematical model

2.1. Arbitrary Lagrangian/Eulerian (Sharp) Interface (Tracking) Model

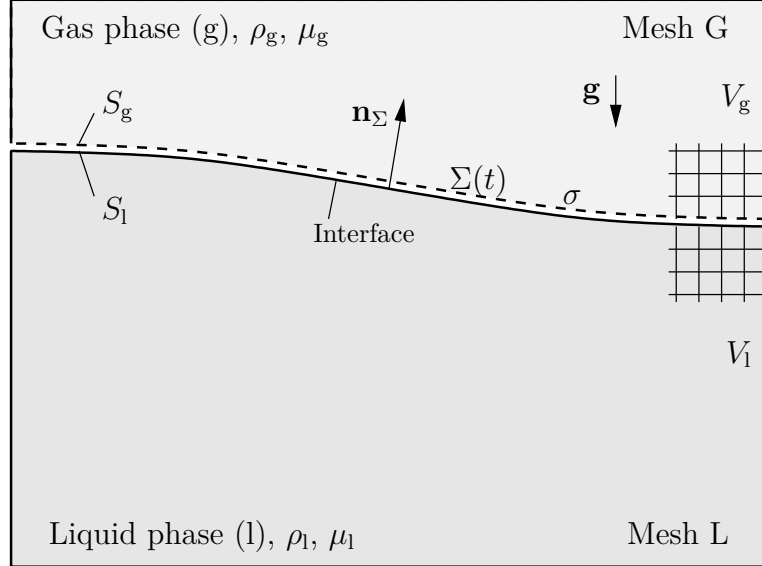


Figure 1: Definition of the solution domain for the ALE-IT method.

We model isothermal flow of two immiscible incompressible fluids, schematically shown in fig. 1, e.g. as a liquid and a gas phase separated by a sharp interface $\Sigma(t)$. Appropriate boundary conditions

are then enforced at the fluid interface $\Sigma(t)$, see [31]. We only briefly outline the model, the reader is additionally referred to [15] for more details.

Isothermal flow of an incompressible Newtonian fluid inside an arbitrary moving control volume V bounded by a closed surface $S := \partial V$, i.e. S is the boundary of the finite volume, moving with the boundary velocity \mathbf{v}_s is governed by the mass and linear momentum conservation laws:

$$\oint_S \rho \mathbf{n} \cdot \mathbf{v} \, dS = 0, \quad (1)$$

$$\frac{\partial}{\partial t} \int_V \rho \mathbf{v} \, dV + \oint_S \mathbf{n} \cdot \rho(\mathbf{v} - \mathbf{v}_s) \mathbf{v} \, dS = \oint_S \mathbf{n} \cdot \boldsymbol{\tau} \, dS - \int_V \nabla p \, dV, \quad (2)$$

where \mathbf{n} is the outward pointing unit normal on S , ρ is the fluid density, \mathbf{v} is the fluid velocity, \mathbf{v}_s is the velocity of surface S , and $\boldsymbol{\tau}$ is the viscous stress tensor which together with the thermodynamic pressure p' makes the Cauchy stress tensor $\mathbf{T} = -p' \mathbf{I} + \boldsymbol{\tau}$. The dynamic pressure in Eq. (2) is defined as

$$p = p' - \rho \mathbf{g} \cdot \mathbf{r}, \quad (3)$$

where \mathbf{g} is the gravitational acceleration vector and \mathbf{r} is the position vector. Furthermore, the viscous stress tensor of the Newtonian fluid is given by

$$\boldsymbol{\tau} = \eta(\nabla \mathbf{v} + \nabla \mathbf{v}^T), \quad (4)$$

where η is the dynamic viscosity.

The relationship between the rate of change of the volume V and the velocity \mathbf{v}_s is defined by the *geometric (space) conservation law* (GCL, see [27, 8]):

$$\frac{\partial}{\partial t} \int_V dV - \oint_S \mathbf{n} \cdot \mathbf{v}_s \, dS = 0. \quad (5)$$

The formulation of the above mathematical model is a well-known ALE formulation.

2.2. Interface coupling conditions

If fluid phases are immiscible, fluid flow eqs. (1) and (2) can be applied for each phase separately, while on the interface the proper boundary conditions must be used. The relation between fluid velocities on the two sides of the interface is determined by the *kinematic condition*, which states that the velocity must be continuous across the interface:

$$\mathbf{v}_l = \mathbf{v}_g, \quad (6)$$

where \mathbf{v}_l and \mathbf{v}_g are the fluid velocities at the two sides (e.g. liquid and gas) of the fluid interface.

The dynamic condition follows from the momentum conservation law and states that forces acting on the fluid at the interface are in equilibrium:

$$(p_g - p_l) \mathbf{n}_\Sigma - (\boldsymbol{\tau}_g - \boldsymbol{\tau}_l) \cdot \mathbf{n}_\Sigma = \sigma \kappa \mathbf{n}_\Sigma + \nabla_s \sigma - (\rho_g - \rho_l) (\mathbf{g} \cdot \mathbf{r}) \mathbf{n}_\Sigma, \quad (7)$$

where \mathbf{n}_Σ is the unit normal vector on the interface, which points from the liquid phase to the gas phase, $\kappa = -\nabla_s \cdot \mathbf{n}_\Sigma$ is twice the mean curvature of the interface, σ is the surface tension coefficient

and $\nabla_s \sigma$ is the gradient of the surface tension coefficient, where $\nabla_s = \nabla(\mathbf{I} - \mathbf{n}_\Sigma \mathbf{n}_\Sigma)$ is the surface gradient operator. The last term on the right-hand side of eq. (7) appears due to transformation of the thermodynamic pressure to the dynamic pressure at the interface. The pressure jump across the interface is obtained by taking the normal component of the force balance (eq. (7)):

$$p_g - p_l = \sigma \kappa - 2(\eta_g - \eta_l) \nabla_s \cdot \mathbf{v} - (\rho_g - \rho_l)(\mathbf{g} \cdot \mathbf{r}), \quad (8)$$

The second term on the right-hand side of eq. (8) represents the jump of the normal viscous force across the interface, expressed through the surface divergence of the interface velocity. For example, the normal viscous force at the interface can be expressed as (see [6]):

$$(\mathbf{n}_\Sigma \mathbf{n}_\Sigma) : \boldsymbol{\tau} = 2\eta (\mathbf{n}_\Sigma \mathbf{n}_\Sigma) : \nabla \mathbf{v} = -2\eta \nabla_s \cdot \mathbf{v}, \quad (9)$$

where the following identity, being valid for an incompressible fluid flow ($\nabla \cdot \mathbf{v} = 0$), is used:

$$\nabla \cdot \mathbf{v} = \nabla_s \cdot \mathbf{v} + (\mathbf{n}_\Sigma \mathbf{n}_\Sigma) : \nabla \mathbf{v}. \quad (10)$$

By taking the tangential component of the force balance (eq. (7)) one obtains a relation between the normal derivative of the tangential velocity on the two sides of the interface:

$$\eta_g (\mathbf{n}_\Sigma \cdot \nabla \mathbf{v}_t)_g - \eta_l (\mathbf{n}_\Sigma \cdot \nabla \mathbf{v}_t)_l = -\nabla_s \sigma - (\eta_g - \eta_l) (\nabla_s v_n), \quad (11)$$

where it is taken into account that the tangential component of the viscous force at the interface can be expressed as follows:

$$(\mathbf{n}_\Sigma \cdot \boldsymbol{\tau}) \cdot (\mathbf{I} - \mathbf{n}_\Sigma \mathbf{n}_\Sigma) = \eta (\mathbf{n}_\Sigma \cdot \nabla \mathbf{v}_t + \nabla_s v_n), \quad (12)$$

where $\mathbf{v}_t = (\mathbf{I} - \mathbf{n}_\Sigma \mathbf{n}_\Sigma) \cdot \mathbf{v}$ is the tangential velocity component and $v_n = \mathbf{n}_\Sigma \cdot \mathbf{v}$ is the normal velocity component at the interface. A non-zero gradient $\nabla_s \sigma$ of the surface tension coefficient can occur for example due to a nonuniform distribution of surfactant at the interface or due to the presence of a temperature gradient.

2.3. Surfactant transport

If impact of surfactant on the flow field is to be analyzed, it is necessary to extend the mathematical model by an equation which governs the transport of surfactant in the liquid bulk and an equation which governs the transport of surfactant along the interface. The bulk surfactant transport equation in ALE form read as follows:

$$\frac{\partial}{\partial t} \int_V c dV + \oint_S \mathbf{n} \cdot (\mathbf{v} - \mathbf{v}_s) c dS - \oint_S \mathbf{n} \cdot (D \nabla c) dS = 0, \quad (13)$$

where c is the volume-averaged bulk surfactant concentration and D is the bulk surfactant diffusion concentration.

The governing equation for surfactant transport along a surface patch S attached to the fluid interface ($S \subset \Sigma(t)$) and bounded by a closed curve ∂S which can move along the interface reads:

$$\frac{\partial}{\partial t} \int_S \Gamma dS + \oint_{\partial S} \mathbf{m} \cdot (\mathbf{v} - \mathbf{b}) \Gamma dL - \oint_{\partial S} \mathbf{m} \cdot (D_\Gamma \nabla_s \Gamma) dL = \int_S s_\Gamma dS, \quad (14)$$

where Γ is the surfactant concentration at the interface, Γ_∞ is the saturated surfactant concentration under the given thermodynamic conditions, \mathbf{m} is the outward pointing unit bi-normal on ∂S , \mathbf{b} is the velocity at which the curve ∂S moves along the interface, L is the arc length measured along ∂S , D_s is the diffusion coefficient of the surfactant along the interface and s_Γ is the source/sink of surfactants per unit area due to adsorption and desorption.

For the sake of simplicity, we focus in this paper on the prominent Langmuir's kinetics law [16, 5, 22] for the transfer of surfactant between the bulk and the interface due to adsorption and desorption:

$$s_\Gamma = k_a [c_l(\Gamma_\infty - \Gamma) - \beta\Gamma], \quad (15)$$

where k_a and β are the parameters of the adsorption and desorption kinetics, respectively, and c_l is the value of the bulk surfactant concentration at the interface. The implementation allows for a straightforward extension to cope with other sorption models. The normal derivative of bulk surfactant concentration at the interface is given by following expression:

$$(\mathbf{n} \cdot \nabla c)_\Sigma = -\frac{s_\Gamma}{D}. \quad (16)$$

In order to account for the surfactant bulk-interface mass transfer balance (eq. (16)), the normal derivative of the surfactant concentration at the interface needs to be calculated with sufficient accuracy. Due to convection along the interface and typically small surfactant diffusivities, extremely thin boundary layers appear and make this calculation a challenging step. At this point, use of subgrid-scale modeling for improved flux calculation as described in section 4 is beneficial.

The surface tension is related to the surfactant concentration on the interface and given for the Langmuir sorption model with its adsorption isotherm by the following equation of state

$$\sigma = \sigma_0 + \mathcal{R}T\Gamma_\infty \ln \left(1 - \frac{\Gamma}{\Gamma_\infty} \right), \quad (17)$$

where σ_0 is the surface tension of a clean interface, \mathcal{R} is the universal gas constant and T is the temperature [16, 5, 22]. Equation (17) can also be written as

$$\sigma = \sigma_0 \left[1 + \beta_s \ln \left(1 - \frac{\Gamma}{\Gamma_\infty} \right) \right], \quad (18)$$

where $\beta_s = \frac{\mathcal{R}T\Gamma_\infty}{\sigma_0}$ is the elasticity number. For the test case described in section 6.3 we added a linear equation of state:

$$\sigma = \sigma_0 \left(1 + \beta_s \frac{\Gamma}{\Gamma_\infty} \right). \quad (19)$$

3. Finite Volume and Finite Area discretisation and equation-system solution

3.1. Discretisation of the computational domain

The cell-centered Finite Volume Method (FVM, [31]) is used to discretise the bulk fluid models (volumetric transport equations) and the face-centered Finite Area Method (FAM, [31]) is used to discretise the surfactant transport model, a transport equation on the fluid interface (moving surface). The finite volume/area discretisation is based on the integral form of the conservation

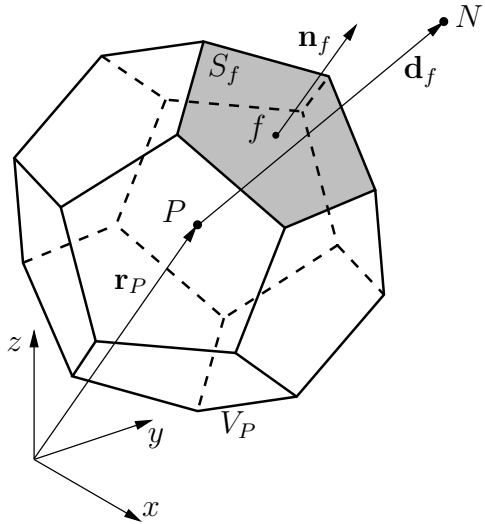


Figure 2: Polyhedral control volume (cell) and the notation used (adopted from [31])

equation over a fixed or moving control volume/area. The discretisation procedure is divided into two parts: discretisation of the computational domain and the equation discretisation. Here we provide a brief description of both discretisation methods together with a description of the interface tracking method, while more details can be found in [31, 29, 28].

The time interval is split into a finite number of time-steps Δt and the equations are solved in a time-marching manner. The computational space is divided into a finite number of polyhedral control volumes (CV) or cells bounded by polygons. The cells do not overlap and fill the spatial domain completely. Figure 2 shows a polyhedral control volume V_P around the computational point P located in its centroid, face f with area S_f , face unit normal vector \mathbf{n}_f and the centroid N of a neighboring CV sharing the face f . The geometry of the CV is fully determined by the position of its vertices.

In case the solution domain is changing in time, e.g., when the fluid interface deforms, the finite volume mesh is adjusted to the time-varying position or shape of the solution domain boundaries using a deforming mesh approach. The internal CV-vertices are moved based on the prescribed motion of the boundary vertices, while the topology of the mesh stays unchanged. In the implemented moving mesh interface tracking solver, a finite-volume automatic mesh motion solver is applied, where the Laplace equation is solved for mesh-point displacements with variable diffusion coefficient, using the polyhedral unstructured cell-centered FVM.

The polygonal cell-faces which coincide with the interface constitute the finite area mesh on which the surfactant transport equation is discretised. Figure 3 shows a sample polygonal control area S_P around the computational point P located in its centroid, the edge e , the edge length L_e , the edge unit bi-normal vector \mathbf{m}_e and the centroid N of the neighbouring control area sharing the edge e . The bi-normal \mathbf{m}_e is perpendicular to the edge normal \mathbf{n}_e and to the edge vector \mathbf{e} .

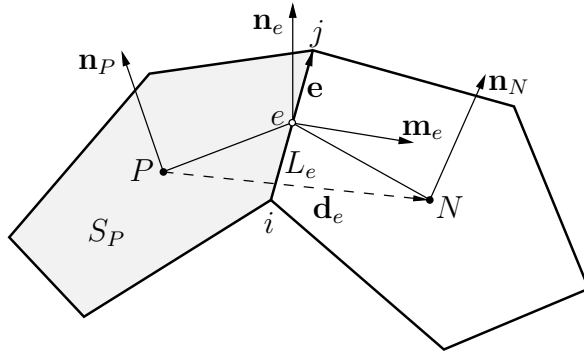


Figure 3: Polygonal control area.

3.2. Discretisation of volumetric equations

The second-order collocated FV discretisation of an integral conservation equation transforms the surface integrals into sums of face integrals and approximates them and the volume integrals to the second order accuracy by using the mid-point rule. The spatially discretised form of the momentum eq. (2) for the moving control volume V_P reads:

$$\begin{aligned} & \frac{\partial (\mathbf{v}_P V_P)}{\partial t} + \sum_f (\dot{V}_f - \dot{V}_{s,f}) \mathbf{v}_f \\ &= \sum_f \nu_f [\mathbf{n} \cdot (\nabla \mathbf{v})]_f S_f + (\nabla p)_P V_P, \end{aligned} \quad (20)$$

where the subscripts P and f represent the cell-center and face-center values. The volume flow rate due to fluid flow through the cell-face, $\dot{V}_f^{n+1} = (\mathbf{n} \cdot \mathbf{v} S)_f^{n+1}$ must satisfy the discretised mass conservation law, where the superscript $n+1$ represents the new time-step, while the volume flux due to grid motion, $\dot{V}_{s,f}^{n+1}$, must satisfy the discretised GCL, eq. (5). The evaluation of the mesh-face volume fluxes is described in [11, 29].

The face-center values of all dependent variables are calculated using linear interpolation of the neighbouring cell-center values. The exception is the face value of the dependent variable in the convection term $[\mathbf{v}_f$ in eq. (20)] which must be calculated using some of the bounded convection discretisation schemes available in OpenFOAM.

The face-normal derivative of the velocity $[\mathbf{n} \cdot \nabla \mathbf{v}]_f$ is discretised using the linear scheme with non-orthogonal and skewness correction (see fig. 2):

$$(\mathbf{n} \cdot \nabla \mathbf{v})_f = \frac{\mathbf{v}_N - \mathbf{v}_P}{d_{n,f}} + \frac{\mathbf{k}_N \cdot (\nabla \mathbf{v})_N - \mathbf{k}_P \cdot (\nabla \mathbf{v})_P}{d_{n,f}}, \quad (21)$$

where $d_{n,f} = \mathbf{n}_f \cdot \mathbf{d}_f$, $\mathbf{k}_P = (\mathbf{I} - \mathbf{n}_f \mathbf{n}_f) \cdot (\mathbf{r}_f - \mathbf{r}_P)$ and $\mathbf{k}_N = (\mathbf{I} - \mathbf{n}_f \mathbf{n}_f) \cdot (\mathbf{r}_N - \mathbf{r}_f)$. The first term on the right-hand side of eq. (21) is treated implicitly, while the correction term is treated explicitly.

The cell-face volumetric fluid flux in the non-linear convection term is treated explicitly after the discretisation, i.e. its values from the previous iteration are used. The cell-center gradient of the dependent variables used for the calculation of the explicit source terms and the non-orthogonal

correction in eq. (21), is obtained by using the least-squares fit [7]. This method produces a second-order accurate gradient irrespective of the mesh quality.

The **temporal discretisation** of all equations is performed by using the second-order accurate implicit three time level scheme [11] referred to as the backward scheme in OpenFOAM. All terms of eq. (20) are evaluated at the new time instance $t^{n+1} = t^n + \Delta t$ and the temporal derivative is discretised by using two old-time levels:

$$\left(\frac{\partial \mathbf{v}}{\partial t}\right)^{n+1} = \frac{3\mathbf{v}^{n+1} - 4\mathbf{v}^n + \mathbf{v}^{n-1}}{2\Delta t}, \quad (22)$$

where $\mathbf{v}^{n+1} = \mathbf{v}(t^n + \Delta t)$, $\mathbf{v}^n = \mathbf{v}(t^n)$ and $\mathbf{v}^{n-1} = \mathbf{v}(t^n - \Delta t)$. One can also use other temporal discretisation schemes available in OpenFOAM.

When eqs. (21) and (22) are substituted into eq. (20) and the convection discretisation scheme is applied, the discretised form of the momentum eq. (2) can be written in the form of a linear algebraic equation, which for cell P reads:

$$a_P \mathbf{v}_P^{n+1} + \sum_N a_N \mathbf{v}_N^{n+1} = \mathbf{r}_P + (\nabla p)_P, \quad (23)$$

where the diagonal coefficient a_P , the off-diagonal coefficients a_N and the source term \mathbf{r}_P can be found in [29].

The mathematical model of fluid flow is solved using a segregated solution procedure where the discretised momentum equation is solved decoupled from the discretised pressure equation. The discretised pressure Poisson equation, obtained by combining the discretised momentum and continuity equations, reads:

$$\sum_f \left(\frac{1}{a}\right)_f (\mathbf{n} \cdot \nabla p)_f^{n+1} S_f^{n+1} = \sum_f \mathbf{n}_f^{n+1} \cdot \left(\frac{\mathbf{H}}{a}\right)_f S_f^{n+1}, \quad (24)$$

where the $(1/a)_f$ and $(\mathbf{H}/a)_f$ terms are calculated by using the temporally consistent Rhie-Chow interpolation procedure proposed in [29].

The face normal derivative of the pressure at the left hand side of eq. (24) is discretised using eq. (21) applied on the pressure field. The absolute volume fluid flux \dot{V}_f^{n+1} through the cell face f is calculated as follows:

$$\dot{V}_f^{n+1} = \mathbf{n}_f^{n+1} \cdot \left[\left(\frac{\mathbf{H}}{a}\right)_f - \left(\frac{1}{a}\right)_f (\nabla p)_f^{n+1} \right] S_f^{n+1}. \quad (25)$$

Volume flux calculated in this manner will satisfy the discretised continuity equation if the pressure field satisfies the pressure eq. (24).

3.3. Discretisation of surface equations

Applying a second-order collocated finite area method, the surfactant transport eq. (14) can be discretised on the moving control area S_P (see fig. 3) as follows:

$$\frac{\partial (\Gamma_P S_P)}{\partial t} + \sum_e (\mathbf{m} \cdot \mathbf{v})_e L_e \Gamma_e = \sum_e D_{\Gamma,e} (\mathbf{m} \cdot \nabla_s \Gamma)_e L_e + (s_{\Gamma})_P S_P, \quad (26)$$

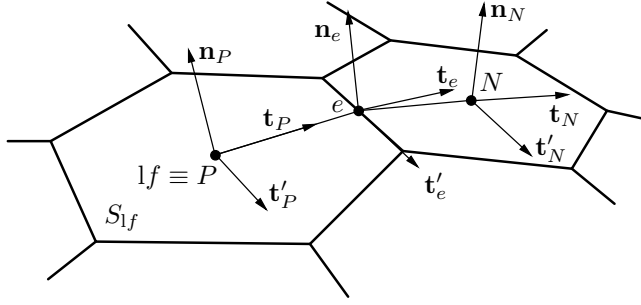


Figure 4: Edge-based local orthogonal coordinate system whose axis are aligned with the orthogonal unit vectors \mathbf{n} , \mathbf{t} and \mathbf{t}' , where vector \mathbf{t} is tangential to the geodetic line \overline{PeN}

where the subscripts P and e represent the face-center and edge-center values, and it is assumed that finite-area points move in normal direction which means that $(\mathbf{m} \cdot \mathbf{b})_e = 0$.

The edge-center tangential velocity \mathbf{v}_t is calculated using following linear interpolation formula:

$$\mathbf{v}_{t,e} = (\mathbf{T}_e)^T \cdot [e_x \mathbf{T}_P \cdot \mathbf{v}_{t,P} + (1 - e_x) \mathbf{T}_N \cdot \mathbf{v}_{t,N}]. \quad (27)$$

where e_x is the interpolation factor which is calculated as the ratio of the geodetic distances \overline{eN} and \overline{PeN} (see fig. 3):

$$e_x = \frac{\overline{eN}}{\overline{PeN}}, \quad (28)$$

and \mathbf{T}_P , \mathbf{T}_N and \mathbf{T}_e are the tensors of transformation from the global Cartesian coordinate system to the $(\mathbf{t}'_e, \mathbf{t}_e, \mathbf{n}_e)$ edge-based local coordinate system defined in fig. 3. The convection term in eq. (26) is discretised using the linear upwind discretisation scheme by taking into account geodetic distances between the neighbouring control area centers. The diffusion term is discretised using the central differencing scheme with non-orthogonal correction [14]:

$$(\mathbf{m} \cdot \nabla_s \psi)_e = \underbrace{|\Delta_e| \frac{\psi_N - \psi_P}{L_{PN}}}_{\text{Orthogonal contribution}} + \underbrace{\mathbf{k}_e \cdot (\nabla_s \psi)_e}_{\text{Non-orthogonal correction}}, \quad (29)$$

where $\mathbf{k}_e = \mathbf{m}_e - \Delta_e$, $\Delta_e = \frac{\mathbf{t}_e}{\mathbf{t}_e \cdot \mathbf{m}_e}$, L_{PN} is the geodetic distance \overline{LeP} and \mathbf{t}_e is the unit tangential vector to the geodetic line \overline{PeN} at the point e (see fig. 4).

3.4. Interface tracking procedure

The numerical modelling of the two-phase fluid flow with a sharp interface is performed using a moving mesh interface tracking procedure. The computational mesh consists of two separate parts, where each of the meshes covers only one of the considered two fluid phases, see fig. 1. The two meshes are in contact over two geometrically equal surfaces, S_l and S_g , at the boundary between the phases, i.e. the interface. Surface S_l represents the liquid side of the interface, and surface S_g represent the gas side of the interface. Each surface is defined by a set of boundary faces, see fig. 5, where each face lf on the surface S_l has a corresponding geometrically equal face gf on the surface S_g . Matching of the two meshes at the interface is assumed in order to make the explanation of the interface tracking method clearer, and is not required in general.

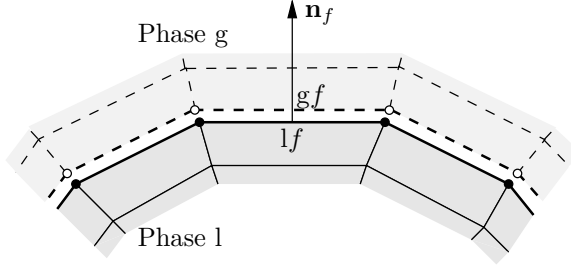


Figure 5: Representation of the interface with the mesh boundary faces.

Coupling of flow equations between fluid phases is performed by applying adequate boundary conditions at the boundary faces which define the side l and g of the interface. At the side l the pressure p_l and normal velocity derivative $(\mathbf{n} \cdot \nabla \mathbf{v})_l$ are specified, while at the side g the velocity \mathbf{v}_g is specified and normal derivative of dynamic pressure is set to zero, $(\mathbf{n} \cdot \nabla p)_g = 0$. The boundary conditions are calculated using the kinematic and dynamic conditions as follows:

1. The value of dynamic pressure specified on the face l_f (see fig. 5) is calculated from the dynamic pressure at the face g_f using eq. (8) as follows:

$$p_{lf} = p_{gf} - (\rho_l - \rho_g) \mathbf{g} \cdot \mathbf{r}_{lf} - (\sigma\kappa)_{lf} - 2(\eta_l - \eta_g) (\nabla_s \cdot \mathbf{v})_{lf}, \quad (30)$$

where p_{gf} is the dynamic pressure at the face g_f calculated by extrapolation from the fluid g, and \mathbf{r}_{lf} is the position vector of the face center l_f . The surface divergence of the velocity vector $(\nabla_s \cdot \mathbf{v})_{lf}$ at l_f is calculated using the surface Gauss integral theorem [32]. The procedure for calculating the surface force $(\sigma\kappa)_{lf}$ is described later in this section.

2. The normal velocity derivative specified at l_f is calculated from the normal velocity gradient at g_f using eq. (11), as follows:

$$\begin{aligned} (\mathbf{n} \cdot \nabla \mathbf{v})_{lf} &= \frac{\eta_g}{\eta_l} (\mathbf{I} - \mathbf{n}_{lf} \mathbf{n}_{lf}) \cdot \left[\mathbf{n}_{lf} \cdot (\nabla \mathbf{v})_{gf} \right] \\ &+ \frac{1}{\eta_l} (\nabla_s \sigma)_{lf} - \mathbf{n}_{lf} (\nabla_s \cdot \mathbf{v})_{lf} \\ &+ \frac{(\eta_g - \eta_l)}{\eta_l} (\nabla_s \mathbf{v}_n)_{lf}, \end{aligned} \quad (31)$$

where $\mathbf{n}_{lf} = -\mathbf{n}_{gf}$ is the unit normal of the face l_f . Equation (31) is derived using the identity $\mathbf{n} \cdot \nabla \mathbf{v} + \mathbf{n} (\nabla_s \cdot \mathbf{v}) = (\mathbf{I} - \mathbf{n} \mathbf{n}) \cdot (\mathbf{n} \cdot \nabla \mathbf{v})$. The surface gradient of the normal velocity component $(\nabla_s \mathbf{v}_n)_{lf}$ at l_f is calculated using the surface Gauss integral theorem. Calculating the tangential surface force $(\nabla_s \sigma)_{lf}$ is described later in this section.

3. According to the kinematic condition (6), the tangential velocity component specified on g_f is transferred from l_f :

$$(\mathbf{v}_t)_{gf} = (\mathbf{v}_t)_{lf}. \quad (32)$$

The normal velocity component specified on g_f is calculated from the condition of zero net mass flux, $(\dot{V}_{gf} - \dot{V}_{g_f}) = 0$, i.e.

$$(\mathbf{v}_n)_{gf} = -\frac{\dot{V}_{gf}}{S_{gf}} \mathbf{n}_{lf}, \quad (33)$$

where \dot{V}_{gf} is the volume flux of the face gf . Since the displacement of mesh points on the side g is equal to the displacement on the side l of the interface, $\mathbf{u}_{gi} = \mathbf{u}_{li}$, the same is valid for the volume fluxes of the faces lf and gf :

$$\dot{V}_{gf} = \dot{V}_{lf}. \quad (34)$$

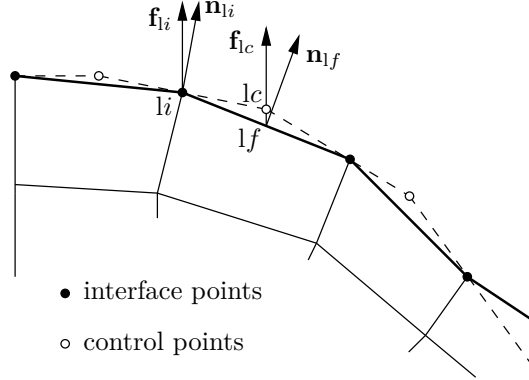


Figure 6: Definition of the interface using control points.

The specification of interface boundary conditions using the above procedure is done at the beginning of each outer iteration. In general, at the end of an outer iteration, the net volume flux through the boundary side l is different from zero, i.e.

$$[\dot{V}_{lf}^p - (\dot{V}_s)_{lf}^p] \neq 0, \quad (35)$$

where \dot{V}_{lf}^p is the fluid volume flux through the face lf and $(\dot{V}_s)_{lf}^p$ is the cell-face volume flux through the same face, both obtained in the previous outer iteration. In order to correct the net volume flux, the interface points must be moved to accomplish the following volume flux corrections:

$$\dot{V}'_{lf} = [\dot{V}_{lf}^p - (\dot{V}_s)_{lf}^p]. \quad (36)$$

The displacement of the interface points is calculated based on the procedure proposed by [21], where a control point lc is attached to the each face lf at the side l of the interface as is shown in fig. 6. The corrected position of the interface points is calculated using the following procedure:

1. Calculate the volume $\delta V'_{lf}$ which face lf sweeps on the way from the current to the corrected position in order to cancel the net mass flux:

$$\delta V'_{lf} = \frac{2}{3} \dot{V}'_{lf} \Delta t, \quad (37)$$

where \dot{V}'_{lf} is the volume flux correction for face lf , eq. (36).

2. Using the above, the displacement of control points in the direction \mathbf{f}_{lc} is:

$$h'_{lc} = \frac{\delta V'_{lf}}{S_{lf}^p \mathbf{n}_{lf}^p \cdot \mathbf{f}_{lc}}, \quad (38)$$

where S_{lf}^p and \mathbf{n}_{lf}^p are the area and unit normal of the face lf in the previous iteration and \mathbf{f}_{lc} is the control point displacement direction. The new corrected positions of the control points are calculated according to the following expression:

$$\mathbf{r}_{lc}^n = \mathbf{r}_{lc}^p + h'_{lc} \mathbf{f}_{lc}, \quad (39)$$

where \mathbf{r}_{lc}^p is the position vector of the control point lc before the correction.

3. The new position of the interface mesh point li is obtained by projection to the plane which is laid over the corresponding control points using the least square method.

3.5. Calculation of interface curvature and surface tension

Regardless of the approach used for tracking the interface between the phases in a multiphase fluid flow, the implementation of surface tension is always demanding.

Let us assume the interface is discretised with an unstructured surface mesh consisting of arbitrary polygonal control areas. The surface tension force acting on the control area S_{lf} (see fig. 7) can be expressed by the following equation:

$$\mathbf{F}_{lf}^\sigma = \oint_{\partial S_{lf}} \mathbf{m} \sigma \, dL = \sum_e \int_{L_e} \mathbf{m} \sigma \, dL = \sum_e \sigma_e \mathbf{m}_e L_e, \quad (40)$$

where σ_e and \mathbf{m}_e are the surface tension and bi-normal unit vector at the center of the edge e and L_e is the length of the edge e . If the total surface tension force for each control area in the mesh is calculated using eq. (40), then the total surface tension force for a closed surface will be exactly zero if the unit bi-normals \mathbf{m}_e for two control areas sharing the edge e are parallel and have opposite direction.

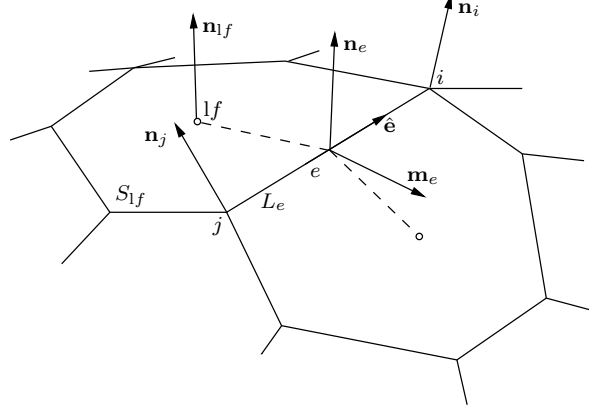


Figure 7: Control area S_{lf} at the interface.

It remains to decompose the surface tension force \mathbf{F}_{lf}^σ into the tangential component $(\nabla_s \sigma)_{lf}$ used in eq. (31), and the normal component $(\kappa \sigma)_{lf} \mathbf{n}_{lf}$ used in eq. (30). Using the surface Gauss integral theorem, the surface tension force acting on the control area S_{lf} can be expressed by the following equation:

$$\mathbf{F}_{lf}^\sigma = \int_{S_{lf}} \nabla_s \sigma \, dS + \int_{S_{lf}} \kappa \sigma \mathbf{n} \, dS. \quad (41)$$

When the right hand side of eq. (41) is approximated by the mid-point rule and the result of the discretisation is equalised with the right hand side of eq. (40), the following expression is obtained:

$$(\nabla_s \sigma)_{lf} + (\kappa \sigma)_{lf} \mathbf{n}_{lf} = \frac{1}{S_{lf}} \sum_e \sigma_e \mathbf{m}_e L_e. \quad (42)$$

Hence, the tangential component of the surface tension force acting on the control area S_{lf} is equal to the tangential component of the right hand side of eq. (42):

$$(\nabla_s \sigma)_{lf} = \frac{1}{S_{lf}} (\mathbf{I} - \mathbf{n}_{lf} \mathbf{n}_{lf}) \cdot \sum_e \sigma_e \mathbf{m}_e L_e \quad (43)$$

and its normal component is equal to the respective normal component:

$$(\kappa \sigma)_{lf} \mathbf{n}_{lf} = \frac{1}{S_{lf}} (\mathbf{n}_{lf} \mathbf{n}_{lf}) \cdot \sum_e \sigma_e \mathbf{m}_e L_e. \quad (44)$$

If the surface tension coefficient is constant ($\sigma = \text{const.}$), eq. (43) will give a tangential component of the surface tension force equal to zero if the normal unit vector of the control area S_{lf} satisfies the following equation:

$$\kappa_{lf} \mathbf{n}_{lf} = \frac{1}{S_{lf}} \sum_e \mathbf{m}_e L_e \quad (45)$$

or, if $\kappa_{lf} \neq 0$:

$$\mathbf{n}_{lf} = \frac{\sum_e \mathbf{m}_e L_e}{|\sum_e \mathbf{m}_e L_e|}. \quad (46)$$

With eqs. (43) to (45) we shall formulate a procedure for the calculation of the surface tension force which ensures that the total surface tension force on a closed surface will be exactly zero. Unfortunately, the fulfilment of this condition is not sufficient for successful application of surface tension forces in the calculation. Specifically, unphysical fluid flow near the interface arises due to local (rather than global) inaccuracy in the calculation of surface tension forces.

From eq. (40) one can see that the accuracy of surface tension force calculation depends on the accuracy of calculation of the bi-normal unit vector \mathbf{m}_e which is calculated using the following expression:

$$\mathbf{m}_e = \hat{\mathbf{e}} \times \frac{\mathbf{n}_i + \mathbf{n}_j}{2}, \quad (47)$$

where $\hat{\mathbf{e}}$ is the unit vector parallel with edge e and \mathbf{n}_i and \mathbf{n}_j are the interface normal unit vectors in points i and j (see fig. 7). Using eqs. (45) and (47) one obtains the exact value of curvature of the control area S_{lf} if the points of the control area lie on the surface of the sphere.

3.6. Solution procedure

Based on the described interface tracking method, one can now define the solution procedure for the Navier-Stokes system on a moving mesh, which may be used for simulating two-phase fluid flow using a moving mesh interface tracking method. The procedure consists of the following steps:

1. For the new time instance $t = t^{n+1}$, initialize the values of all dependent variables with the corresponding values from the previous time instance;

2. Define the displacement directions for the interface mesh points and the control points;
3. Start of outer iteration loop:
 - (a) Update pressure and velocity boundary conditions at the interface;
 - (b) Assemble and solve the discretised momentum equation eq. (20) on the mesh with the current shape of the interface. The pressure field, face mass fluxes and volume fluxes are used from the previous (outer) iteration;
 - (c) The velocity field obtained in the previous step is used for the assembly of the discretised pressure eq. (24). After the pressure equation is solved, new absolute mass fluxes through the cell faces are calculated. The net mass flux through an interface is generally different from zero;
 - (d) In order to compensate the net mass flux obtained in the previous step, the interface displacement is calculated using the interface points displacement procedure defined in the previous section;
 - (e) The interface points displacement is used as a boundary condition for the solution of the mesh motion problem. After mesh displacement, the new face volume fluxes are calculated using the current points positions and the position from the previous time instance;
 - (f) Convergence is checked and if the residual levels and the net mass flux through the interface do not satisfy the prescribed accuracy, the procedure is returned to step (a).
4. If the final time instance is not reached, return to step 1.

4. Subgrid-Scale Model

4.1. Motivation

The simulation of realistic gas-liquid systems is still a huge challenge, e.g. when one would like to simulate an industrial scale bubble column reactor. The nature of this application is multi-scale. One of the smallest scales occurring is that of concentration boundary layers of the rising bubbles at realistic, i.e. high, Schmidt numbers. With conventional FV-methods these scales have to be resolved, what is still unfeasible for an application as the one mentioned above. This motivated the first paper to discuss SGS modeling [1]. In SGS modeling, an analytical function is used to describe the profile of a scalar field inside its boundary layer and to use this SGS information for improved flux computation.

The method has been developed further since and has been applied in the context of Volume of Fluid [34, 13, 4] as well as in interface tracking frameworks [22, 23, 33]. An overview on the state of subgrid-scale modeling was also given by [35]. Recently, the approach was taken up in [12], where local curvature and tangential convection effects have been included.

4.2. Analytical model

The SGS model we implement is based upon analytical solution of a simplified problem, depicted for a bubble in fig. 8. The idea behind the SGS modeling is to zoom in on the interface, so that the curvature gets negligibly small, allowing the analytical model therefore to assume a (locally) flat boundary. This assumption is adequate for scenarios with a concentration boundary layer thickness small in comparison to the radius of curvature of the given boundary.

At the interface Σ of the model problem (see fig. 8), a constant and homogeneous concentration c_Σ is prescribed, which can be computed from Henry's law under the sensible assumption of a well-mixed gas-side concentration, as is pointed out by [4].

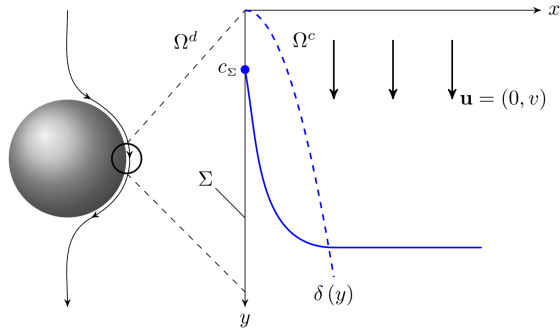


Figure 8: The simplified model for species transfer across a bubble surface. [34] adapted from [4]

The velocity in the substitute model problem is parallel to the interface. No velocity gradient normal to the boundary exists in the model problem ($\partial v / \partial x = 0$). There could be a non-zero gradient in the boundary-parallel direction, in which case the boundary layer thickness δ in eq. (49) would change accordingly. There is no velocity component normal to the boundary.

In the application within ALE-IT, the boundary geometry and the velocity field have to be resolved. In a co-moving reference frame, the interface neighbouring cell's velocity should be nearly parallel to the interface and with the assumption of zero interface-normal velocity gradient the next cells velocity should be nearly identical to it. When a thin scalar boundary layer exists, the SGS can model the scalar fluxes normal to the boundary without resolving the scalar boundary layer itself.

Further assumptions of the substitute problem are a given, constant value (e.g. zero concentration) upstream ($y < 0$) of the domain and far away from the boundary ($x \rightarrow \infty$) as well as negligible diffusion in streamwise direction. We also assume quasi-steadiness and the transported scalar being passively transported.

Applying these assumptions to the advection-diffusion eq. (13) with the sorption term $s^\Sigma + [\![\mathbf{j} \cdot \mathbf{n}_\Sigma]\!] = 0$ on $\Sigma(t)$ and Fick's law $\mathbf{j} = -D\nabla c$ and ν being the boundary-parallel velocity, lead to the expression

$$\nu \frac{\partial c}{\partial y} = D \frac{\partial^2 c}{\partial x^2} \quad \text{for } x > 0 \text{ and } y > 0 \quad (48)$$

with the boundary conditions

$$c(x, y = 0) = c_\infty, \quad c(x \rightarrow \infty, y > 0) = c_\infty \quad \text{and} \quad c(x = 0, y > 0) = c|_\Sigma.$$

The analytical solution to this problem is

$$c(x, y) = c|_\Sigma + (c_\infty - c|_\Sigma) \cdot \text{erf} \left(\frac{x}{\delta(y)} \right) \quad \text{with } \delta(y) = \sqrt{4Dy/\nu}. \quad (49)$$

The boundary layer thickness δ is considered a free parameter, which in IT will be fitted for each interface attached cell individually as described in section 4.3.2. The fitting selects the locally best approximation from the family of given error-functions in eq. (49).

From the analytical solution for the fitted parameter, we can approximate a more accurate boundary-normal gradient of the scalar concentration at the interface as well as at the first cell faces normal to the boundary, x_f in fig. 9. These gradients are used to scale the convective and diffusive scalar fluxes in the Finite Volume discretization, keeping the discretization of convective and diffusive operators implicit. Scaling is only applied in interface normal direction and described in detail in sections 4.3.3 and 4.3.4.

Without the SGS, the maximally second-order unstructured Finite Volume convective and diffusive fluxes are underestimated at the interface and overestimated at the first cell faces normal to the boundary. Figure 9 visualizes the linear gradient calculation in red and the actual gradients at the interface and the first cell faces normal to the boundary with the dashed blue lines.

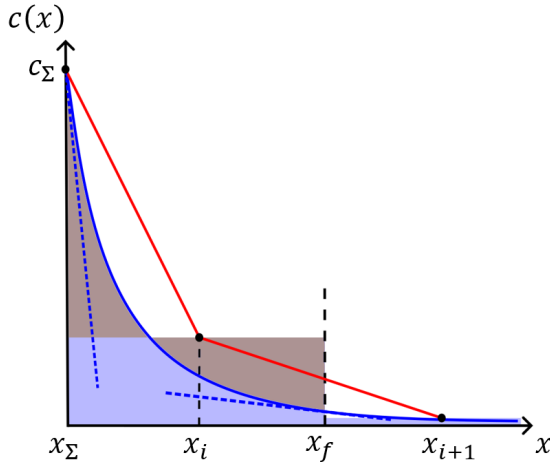


Figure 9: The concentration profile and linear/corrected gradient next to a boundary. Adapted from [34].

Note that in the algorithm the concentration in the first cell is not altered by the SGS. Instead the gradients are used to scale the diffusivities at the respective locations, as described in sections 4.3.3 and 4.3.4.

Details of the SGS model can be found in [4, 34, 23]. It has been applied to VoF by [34], where the implementation becomes more complicated.

4.3. Algorithm

4.3.1. Equation discretization in finite volume solvers

The species transport eq. (13) is discretised using the unstructured Finite Volume Method, e.g. using the backward scheme as described above for Navier-Stokes equations,

$$\frac{3c_P^{n+1}V_P^{n+1} - 4c_P^nV_P^n + c_P^{n-1}V_P^{n-1}}{\Delta t} + \sum_f \Phi_f c_f^{n+1} = \sum_f D_f (\nabla c)_f^{n+1} \cdot \mathbf{S}_f, \quad (50)$$

where V_P is a control volume/cell, $\Phi_f = \mathbf{S}_f \cdot (\mathbf{v} - \mathbf{w})_f$ is the face flux and the superscripts $n+1$, n and $n-1$ symbolize the new, current and preceding timestep. The formula is written for a constant time step size. The subscript P and f represent the value at the cell centers, respectively the face centers.

For the SGS model to take effect in the computation, we will modify the diffusivity coefficient and the face fluxes in the equation above.

4.3.2. Computation of model parameter boundary layer thickness

The model parameter boundary layer thickness δ is computed by iteratively comparing the amount of the scalar in the first cell adjacent to the boundary in the simulation, $\bar{\eta}_c$, with the amount that would be contained in said cell for a given δ , η_{SGS} . In fig. 9 both light brown areas have to be the same size or the area enclosed by the real concentration profile and the cell centered FV-value has to be the same. Mathematically this is being expressed in this expression:

$$\bar{\eta}_c = \frac{\bar{c} - c_{|\Sigma}}{c_{\infty} - c_{|\Sigma}} \stackrel{!}{=} \frac{1}{V} \int_V \eta(x/\delta) dV = \eta_{SGS} \quad (51)$$

with

$$\eta(x, y) = \frac{c(x, y) - c_{|\Sigma}}{c_{\infty} - c_{|\Sigma}} = \text{erf}(x/\delta(y)). \quad (52)$$

Using the derivative of η_{SGS} with respect to δ , as described in [23], we use a Newton-bisection method until eq. (51) is fulfilled within a given tolerance. For details like the initial value and the algorithm in detail the reader is referred to the previously cited article.

For both, the advective and diffusive flux, the same idea is utilized: the scaling of the fluxes according to the boundary layer thickness and therefore the theoretical values given by the SGS.

4.3.3. Computation of diffusive fluxes

With D being the molecular diffusivity, S being the boundary (cell) area and $\partial_n c$ being the surface normal gradient of the scalar c , the diffusive flux F^D is given by

$$F^D = -D \cdot S \cdot \partial_n c. \quad (53)$$

In the following, we will use the superscript SGS to indicate the value is obtained from or modified by the SGS model. The SGS model solves the analytical model for the actual surface normal gradient of c , which will be $(\partial_n c)^{SGS}$. However, to stay implicit and increase numerical stability, the diffusion coefficient is scaled. Therefore, we state that the flux must be equal if computed with the actual gradient or a scaled diffusion coefficient, meaning

$$F^D = -D \cdot S \cdot (\partial_n c)^{SGS} \stackrel{!}{=} D^{SGS} \cdot S \cdot \partial_n c \quad (54a)$$

which can be easily re-arranged into

$$D^{SGS} = D \frac{\partial_n c}{(\partial_n c)^{SGS}}, \quad (54b)$$

where D^{SGS} is a scaled diffusivity value that leads to the same flux, as a calculation with $(\partial_n c)^{SGS}$ would. This scaling is applied to the cell faces at the boundary as well as on the first cell faces normal to the boundary. For both respective locations the diffusivity parameter needs to be modified at the corresponding position, x_{Σ} and x_f in fig. 9. There are exceptions, when the correction is not employed, the details of this can be found in [23].

4.3.4. Computation of advective fluxes

In similar manner to the diffusion, the advective flux is given by

$$F_f^c := c_f^{SGS} F_f = c_f F_f^{SGS} \Phi, \quad (55)$$

where F_f^c is the volumetric flux of the concentration c at the face f , and $F_f := \mathbf{v}_f \cdot \mathbf{S}_f$ is the volumetric flux. Since no convection of the species normal to the interface can take place, the scaling for advective fluxes is only applied to the first cell faces normal to the boundary. Equation (55) analogously to our procedure for the diffusive flux, leads to

$$\Phi^{SGS} = \frac{c^{SGS}}{c} \Phi. \quad (56)$$

Again, an exception handling takes places, of which the details can be found in [23].

5. Software design

5.1. Software design of the SGS model library

The software design is closely related to the model as described in section 4.

The first benefit of our implementation is a strict adherence to the OpenFOAM design principles, which enable easy library extension with new models alternative to the SGS [23] and their Run-Time Selection (RTS) [17] using configuration files. The implementation is depicted in fig. 10, already showing how a new model `newSubGridScaleModel` would be implemented.

The second benefit of our software design is the possibility to apply SGS models to any Partial Differential Equation (PDE) discretized in OpenFOAM, without requiring extensive modification of existing solvers. Our SGS model library can be applied to any part of the domain boundary with a minimal requirement of a prismatic boundary-adjacent mesh with at least three layers of cells in the boundary layer.

Our design of the SGS model implements an OpenFOAM library with a class hierarchy and RTS [17]. A base class which does nothing is present, so an option remains of not using SGS modeling. The SGS model is implemented in a derived class, with virtual functions implementing the functionality from [23]. All functionality needed by the SGS is either accessed from core OpenFOAM libraries or is contained within the SGS model implementation, which ensures the modularity of the SGS model. An alternative SGS model will require similar addressing and geometric mesh information in the boundary layer and the implementation provided in the original SGS model can be re-used.

To enable the user of the SGS a good understanding of the effects of the SGS model and to make accessible insights for further developments of the SGS model, we implemented the possibility to output various SGS model parameters into OpenFOAM `volScalarFields`. These include the model parameter δ or an indication of the exception handling, what represents the reason the SGS model might not be employed. These can easily be inspected visually, an example is given in fig. 16, where the diffusion coefficient after the SGS scaling is visualized. One can see, that on the inflow side, the scaling is strong and of opposite effect for the boundary faces versus the faces between adjacent cell and the next outer cell layer. On the outflow side in contrast, there is little effect to be seen. The third layer represents the un-modified diffusion coefficient. Visualizing multiple operating figures of the SGS enables insights into and deepens the understanding of the simulation case and the effect of the SGS to it.

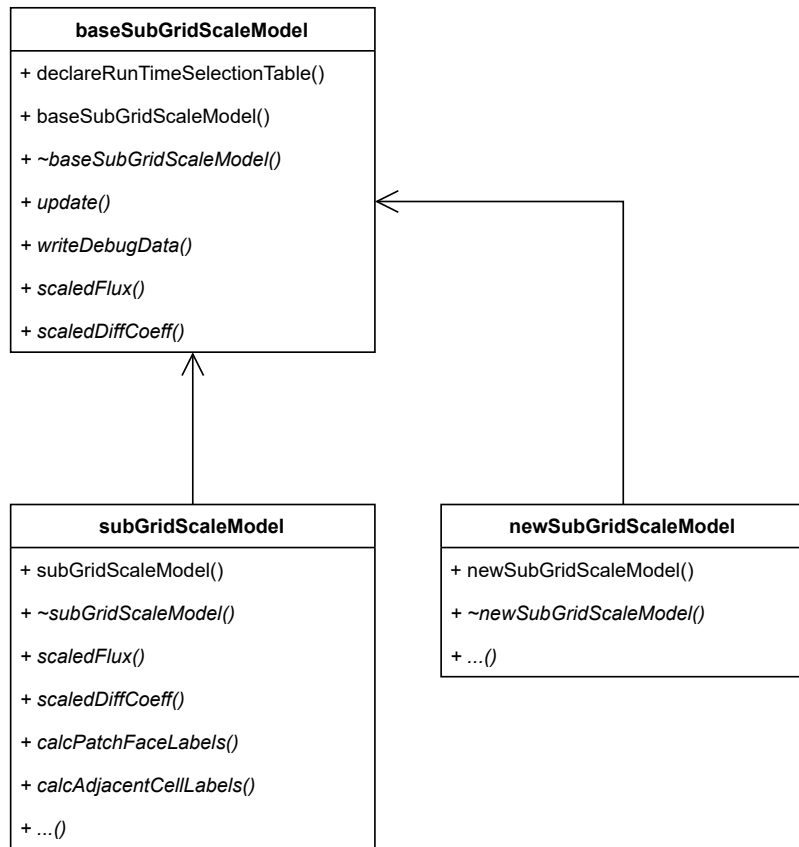


Figure 10: Class diagram of the Subgrid-Scale model, also showing a potential new model

An exemplified code for the modification of the PDE in an OpenFOAM solver for applying an SGS model from our model library is shown in listing 1:

Listing 1: A minimal example of the application of the SGS model to a PDE solver in OpenFOAM.

```

#include "baseSubGridScaleModel.H"
int main(int argc, char *argv[])
{
    ...

    autoPtr<baseSubGridScaleModel> sgsPtr =
        baseSubGridScaleModel::New(transportProperties.subDict("SGS"));

    while (simple.loop())
    {
        Info<< "Time = " << runTime.timeName() << nl << endl;
        while (simple.correctNonOrthogonal())
        {
            // Compute SGS data needed for scaling.
            sgsPtr->update(psi);
            fvScalarMatrix psiEqn
            (
                fvm::ddt(psi)
                + fvm::div(sgsPtr->scaledFlux(phi, psi), psi)
                - fvm::laplacian(sgsPtr->scaledDiffCoeff(D, psi), psi)
                ==
                fvOptions(psi)
            );

            psiEqn.relax();
            fvOptions.constrain(psiEqn);
            psiEqn.solve();
            fvOptions.correct(psi);
        }
        runTime.write();
    }
}

```

The SGS requires some values as user input, that are read from the configuration file *transportProperties* in OpenFOAM, with the relevant SGS sub-dictionary shown in listing 2.

Listing 2: *transportProperties* sub-dictionary for the SGS model

```

SGS
{
    // Choose the SGS model: "SubGridScale" or "inactive"
    type           SubGridScale;

    // patch to apply SGS to
    patchName      freeSurface;

    // far-field concentration
    cInfinity      cInfinity [0 -3 0 0 1 0 0] 0;

    // (optional:) write parameters for visualization
    // of SGS parameters
    visualizeParameters true;

    // (optional:) verbosity level for info statement output (0-3)
    infoLvl        1;
}

```

The SGS model can be activated with the keyword-pair `type SubGridScale` for a mesh boundary patch specified by the keyword `patchName`. Additional required user input is the far-field concentration, defined with the keyword `cInfinity`. Optional parameters are, whether to output additional parameters from the SGS model as an OpenFOAM `volScalarField` and the level of verbosity from 0 to 3 to print to the solver log. 0 corresponds to a quiet mode and 3 prints very extensive information of almost all processes and results within the SGS algorithm and calculations. As these settings affect simulation performance and disk consumption, the first defaults to `false` while the later affects log readability and defaults to 1, which gives limited log-output. These visualizing capabilities as well the rapid info statement level enable insights to the user, but they also help with future model development.

5.2. Automatic testing

We have set up our test cases in a Continuous Integration (CI) pipeline. The pipeline is depicted in figs. 11 and 12. In our approach we follow the practices presented in [18, 19]. This means the tests are run and evaluated automatically in the CI with Jupyter Notebooks. They also produce the results and graphs included in this work. A job in a succeeding stage to the downstream pipeline has been omitted from fig. 12 for the sake of readability. Said job collects and bundles all those artifacts from the two previous stages.

In [18, 19] CI is focused on tests and their automatic evaluation. We have added tests to the CI pipeline, that check certain additional aspects of the repository, like e.g. formatting and the formal correctness of the *CITATION.cff*-file. We also build an image within the CI with OpenFOAM and other needed packages. This job can not be seen in fig. 11, since it is only run once a new OpenFOAM version is available. It is located before the trigger job for the downstream pipelines.

We further expanded the CI to be able to test the code for multiple OpenFOAM versions, which at the moment is being done for the latest three versions OpenFOAM v2312, v2306 and v2212. In feature-branches only the latest version is tested to save resources.

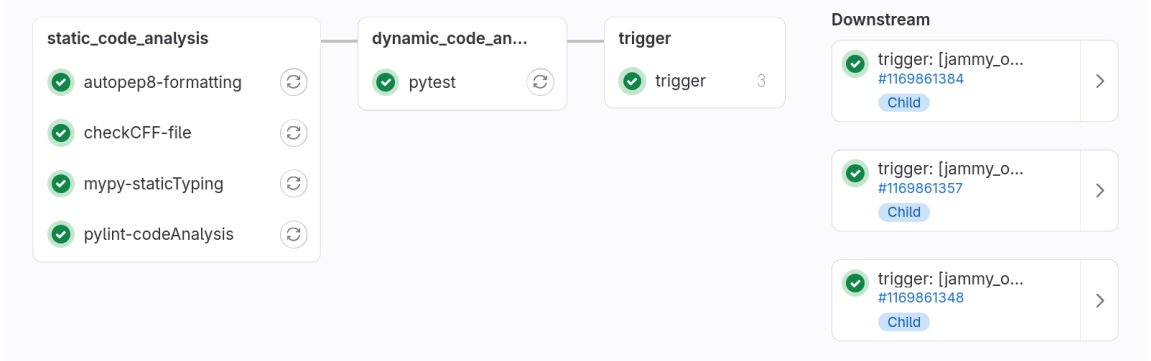


Figure 11: Upstream CI pipeline



Figure 12: Downstream CI pipeline

Another feature of the CI pipeline is the addition of a test, that checks the OpenFOAM log-files for warnings and errors, where tutorials added to the repository are automatically detected and run for a single timestep. This almost ensures, that there are no errors in the set-up of test cases and would also uncover some of errors in the code, that can only be detected, when OpenFOAM is run. The automatisation of this test in finding and running all simulation cases is especially valuable. Since running all of the simulations for only one timestep needs a very limited amount of time it can be checked, that changes in the code don't corrupt any case before committing and pushing to the central repository. The automated finding of cases also prevents forgetting to add a simulation case to the CI (to this testing method) and the automated execution and error finding gently forces all participants of the repository to set up their cases to run flawlessly and fully automatised, e.g. they need to include everything needed to run a case in the *Allrun* script. This ensures all the cases provided with the code can be run without debugging.

Another topic not covered in the previously mentioned references is that for repetitive tasks, like reading dictionary entries, reading files or calculating error norms needed for the evaluation a set of python functions is provided. This set of functions is also tested automatically with the testing framework pytest as part of the CI pipeline and precedes the more computationally expensive OpenFOAM-specific jobs, as can be seen in fig. 11.

6. Results

6.1. Flat plate test case

The smallest test for model development and code verification is what we call the flat plate test case. It implements the assumptions made in section 4.2 and was already implemented by e.g. [23]. The test consists of a flat plate with a prescribed constant concentration of 1 mol/m³. Parallel to this plate a flow is prescribed, that has no interaction with the wall, i.e. there is no velocity

boundary layer or velocity gradient. Initially and in the inflow, the concentration is set to zero, the length of the plate is 0.005 m and the fluid velocity is 0.1 m/s. The timestep of 0.0002 s is used for a physical duration of 0.1 s, which is double the time the fluid needs to be transported through the domain. Figure 13 visualizes the setting.

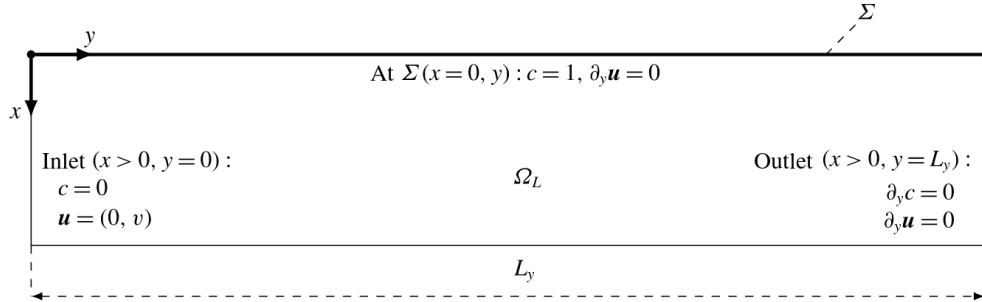


Figure 13: Set-up of the flat plate test. Figure taken from [23].

With the possibilities described in section 5.1, it can be verified that fundamental parts of the algorithm as described in section 4.3 are implemented correctly, like the boundary layer thickness δ and the diffusion correction. Beneficially, there is an analytical solution to this model for comparison. For these reasons the test enables insights into the capabilities of the SGS model and the implementation thereof. This simple test case does circumvent most of the error-handling and also convective flux correction must not have an effect on the outcome.

In fig. 14 the local Sherwood numbers of a parameter study along the boundary surface are displayed. The parameter study has four levels of mesh refinement, where the cell size halves between each execution from $40 \mu\text{m}$ to $5 \mu\text{m}$, four different diffusivity levels spanning four orders of magnitude from $5 \times 10^{-8} \text{ m}^2/\text{s}$ to $5 \times 10^{-11} \text{ m}^2/\text{s}$ and every of these setups is run with and without active SGS model. Taking the length of the plate as reference length L , the Peclet number is within the interval $[10^4, 10^7]$.

It is apparent, how without the SGS model, the Sherwood number cannot be computed in cases with a boundary layer that is small in comparison to the cell size, i.e. when the cell size is big and the diffusivity is small. In contrast to the linear interpolation with the SGS model the Sherwood number is captured reasonably well in all cases. Note in fig. 14, that at some locations the Sherwood number with the application of the SGS model is actually smaller than without it.

6.2. Satapathy-Smith axisymmetric bubble or droplet

The second test case for the SGS model mimics a moving droplet or bubble. It uses the axisymmetric solution of velocity field from Satapathy and Smith in [24] for low Reynolds numbers. The computational domain is a wedge with prescribed velocity. This test case was also implemented by and we take the reference solution from [23]. This test case introduces additional complexity compared to section 6.1, since there is flow non-parallel to the interface, therefore violating some of the assumptions made when deriving the SGS mathematical model, as described in section 4.2. From the visualization capabilities we can see in the rear part of the "bubble" the exception handling partially taking place, as there the concentration rises, not conforming to the assumption of a thin boundary layer (with parallel flow) made in the derivation of the SGS. As in section 6.1 the inflow

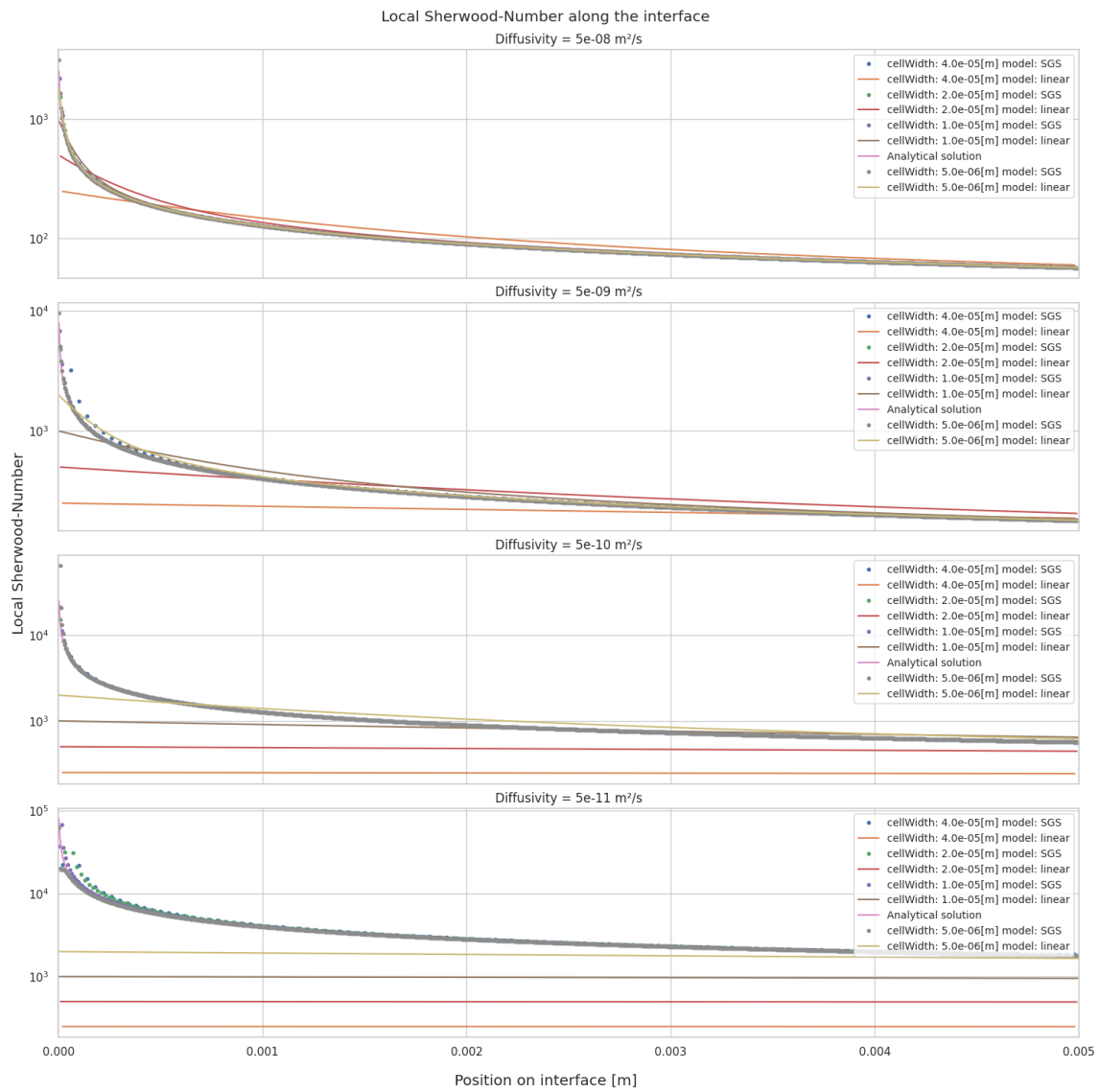


Figure 14: Results for the parameter study over of the flat plate test case

and initial concentration is set to 0 mol/m^3 and the interface is set to have a constant concentration of 1 mol/m^3 . The simulated physical duration is 0.6 s and the results shown here represent the final state.

To see the best results with the SGS, it is important to set the interpolation schemes to `limitedLinear` phi 1.0 for the concentration c and to `linear` for the interpolation of the scaled diffusion coefficient as well as for the flux of U in the `fvSchemes`-file.

We run a parameter study consisting of four different diffusivities from $1 \times 10^{-8} \text{ m}^2/\text{s}$ to $1 \times 10^{-11} \text{ m}^2/\text{s}$, four different mesh resolutions with the meshing parameter $N = [62, 124, 248, 496]$ as the number of faces along the half-circled interface. Every study is run with and without employing the SGS and with a constant timestep of 0.0002 s . The bubble diameter of 2 mm serves as reference length for the Sherwood number. It can be observed from fig. 15 that without deploying the SGS, the local Sherwood number is almost constant and except for the rear part of the bubble too low in case of small diffusivities and coarse meshes. When the mesh resolution is fine and the diffusivity is high, the boundary layer is not as thin (in comparison to the mesh cell size), and therefore the results of linear modeling and SGS modeling are similar.

In fig. 16 the diffusion coefficient after scaling with the SGS is displayed. In the cell layer adjacent to the interface, the diffusion coefficient at the interface is visible, whilst in the next outer cell layer the scaled diffusion coefficient at the faces between interface-adjacent cells and that same cell is visualized. The third row of cells represents the uncorrected diffusion coefficient for reference.

The biggest correction is applied in the front part of the bubble, where the flow impinges onto the interface and the boundary layer is very thin, therefore the derivative in surface normal direction of the concentration is very big. In the rear part of the bubble the boundary layer has grown and the main direction of the flow is no longer parallel to the surface, making the surface concentration gradient in interface-normal direction much smaller and reasonable good represented by linear interpolation. Therefore less correction is needed. To understand what is happening, we would like to point the reader to fig. 9 again.

6.3. Marangoni migration of an air bubble in silicone oil

The velocity of a bubble/droplet within an unbounded fluid subjected to uniform temperature gradient ($\partial T/\partial z$) and zero gravity field ($g = 0$) is defined by following expression [36]:

$$v_{b,YBG}^T = \frac{2}{\left(2 + \frac{\lambda_i}{\lambda_o}\right) \left(2 + 3\frac{\mu_i}{\mu_o}\right)} \frac{R}{\mu_o} \frac{\partial \sigma}{\partial T} \frac{\partial T}{\partial z}, \quad (57)$$

where R is the radius of the bubble, T is the fluid temperature, σ is the surface tension coefficient, μ_i is the dynamic viscosity of the internal fluid, μ_o is the dynamic viscosity of the outside fluid and λ is the thermal conductivity of the fluid.

In the case the Marangoni convection is caused by a specified fixed gradient of surfactant concentration along the interface, the bubble migration velocity can be expressed based on eq. (57) as follows, see [20]:

$$v_{b,YBG}^{\Gamma} = \frac{2}{3 \left(2 + 3\frac{\mu_i}{\mu_o}\right)} \frac{R}{\mu_o} \frac{\partial \sigma}{\partial \Gamma} \frac{\partial \Gamma}{\partial z}, \quad (58)$$

where Γ is the concentration of surfactants at the interface.

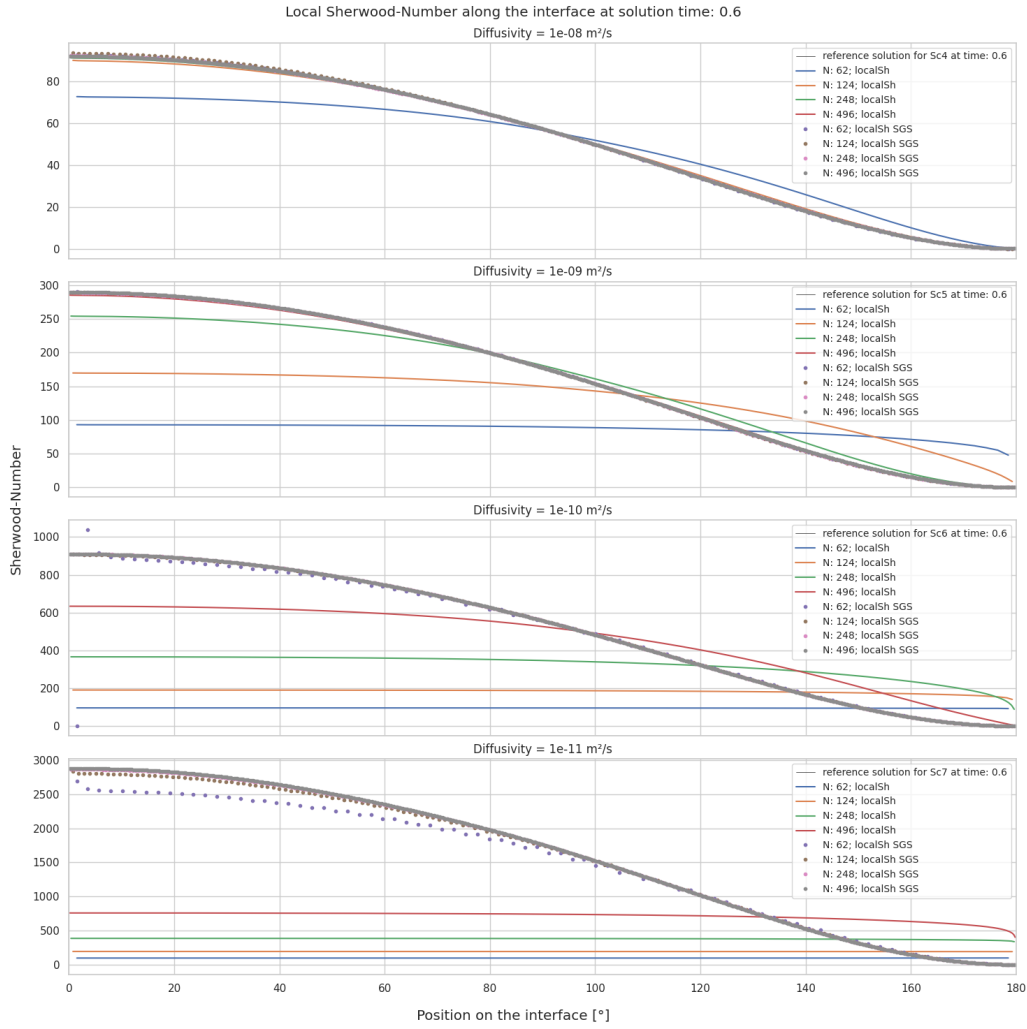


Figure 15: Local Sherwood numbers of a parameter study for Schmidt-numbers from 1×10^4 to 1×10^7

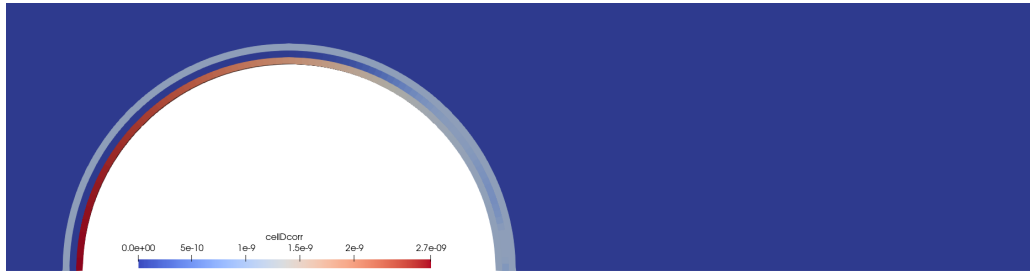


Figure 16: Visualization of corrected diffusion coefficients for the coarsest mesh with a diffusivity of $1 \times 10^{-9} \text{ m}^2/\text{s}$

	$\rho, \text{kg/m}^3$	μ, Pas	$\sigma, \text{N/m}$
Air	1.8×10^{-5}	1.2	0.02
Oil	955	0.191	0.02

Table 1: Properties of air and silicone oil.

A numerical simulation is performed for an air bubble of radius $r_b = 1 \text{ mm}$ moving through the silicone oil. Relevant properties of both phases are listed in table 1. The bubble is assumed to be of spherical shape and rigid and is fixed during the simulation. The spatial computational domain consist of a volume of the spherical bubble filled with air and volume around the bubble bounded by the spherical surface of radius $r = 20r_b$ and filled with silicone oil. The spatial domain is discretised by the unstructured mesh consisting of 979'520 hexahedral cells.

The flow inside and outside of the bubble is driven by Marangoni forces due to the nonuniform distribution of surfactant concentration along the interface, which is fixed during the simulation. The distribution of surfactant along the bubble surface is defined by following linear function:

$$\frac{\Gamma}{\Gamma_\infty} = \frac{z + 2r_b}{L}, \quad (59)$$

where Γ_∞ is the saturated surfactant concentration and L is the length scale, whose value is set to 525 mm. The equation of state is also linear and reads as follows:

$$\sigma = \sigma_s \left(1 - \beta_s \frac{\Gamma}{\Gamma_\infty} \right), \quad (60)$$

where $\beta_s = \frac{\mathcal{R}T\Gamma_\infty}{\sigma_s}$ is the elasticity number which amounts to 2 in this study.

The unsteady computation is performed with time-step size $\Delta t = 0.01 \text{ s}$ using the first order accurate **Euler** temporal discretisation scheme, until steady state is reached. The gradient of the surface tension coefficient as well as the gradients of volume fields is calculated using the least square method. The diffusion terms in the momentum and pressure equations are discretised using the skew-corrected central differencing scheme, while the convective term in the momentum equation is discretised using the linear-upwind scheme. At the outer side of the spatial domain the velocity and normal derivative of pressure are set to zero and at the interface corresponding kinematic and dynamics conditions are enforced.

The bubble rise velocity is calculated based on numerically determined volume flow rates through the faces at the interface as follows:

$$v_b = \frac{\sum_f \text{pos}(\phi_{i,f}) \phi_{i,f}}{\sum_f \text{pos}(\mathbf{k} \cdot \mathbf{S}_{i,f}) (\mathbf{k} \cdot \mathbf{S}_{i,f})}, \quad (61)$$

where $\phi_{i,f}$ is the volume flow rate of the fluid through the face f at the interface, $\mathbf{S}_{i,f}$ is the area vector of the face f at the interface and \mathbf{k} is the unit direction vector of bubble motion. The bubble velocity calculated using eq. (61) based on simulation results amounts to $v_b = 0.001325 \text{ m/s}$, while the corresponding analytical (eq. (58)) gives the migration velocity as $v_{b,YBG}^\Gamma = 0.0013295 \text{ m/s}$. The velocity field inside and around the bubble along the plane $y = 0$ is shown in fig. 17.

6.4. Transport with the interface

We test the framework's ability of adequate transport of a species along an interface with a rotating droplet with a prescribed concentration. The droplet is represented in 2-D. The test setup

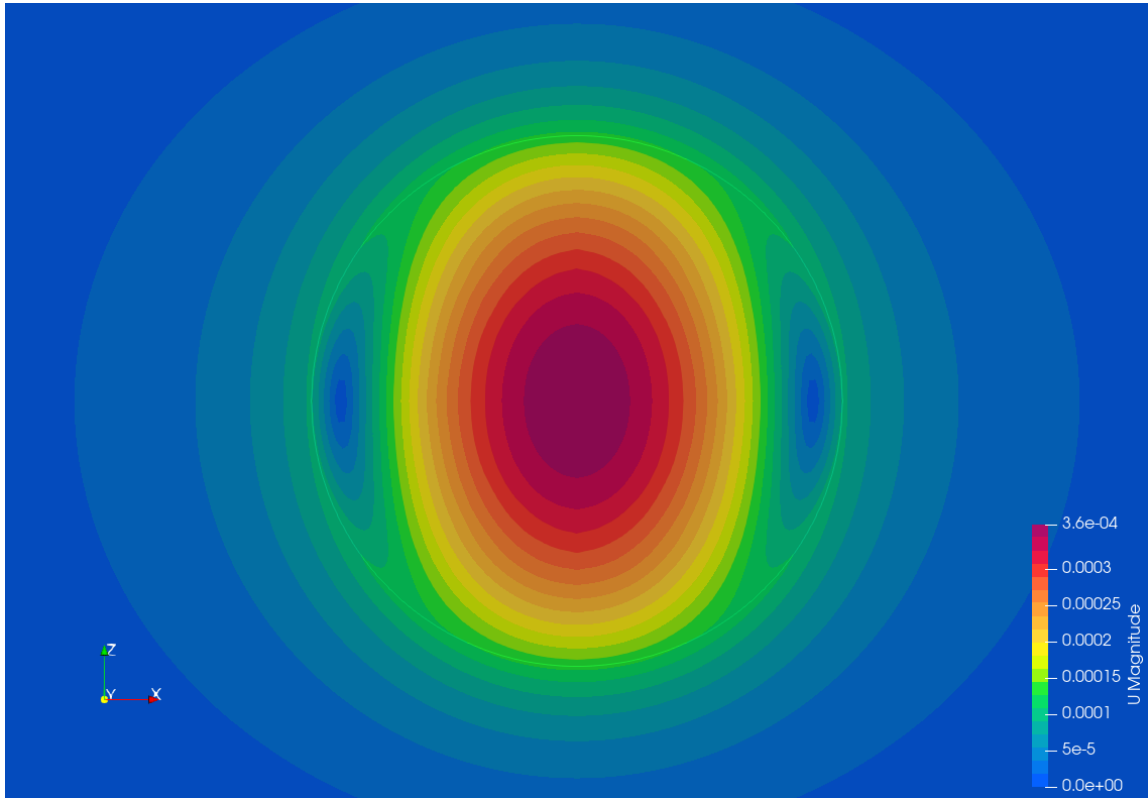


Figure 17: Velocity field inside and around the bubble along the plane $y = 0$ for the bubble marangoni migration case.

follows the test done by [3, 2]. We prescribe the initial concentration distribution and the velocity. For the evaluation we compute one rotation, what equals one second with our prescribed velocity referring to an angular velocity $\omega = 1/s$.

The initial distribution is given by

$$\Gamma(\theta, \tau = 0) = \frac{\cos \theta + 1}{2} \Gamma_0, \quad (62)$$

where Γ is the surface concentration, τ is the time, θ is the angle and Γ_0 is the maximum initial concentration. After a time τ the expected distribution from an analytical approach is given by

$$\Gamma(\theta, \tau) = \frac{e^{-D_I \tau} \cos(\theta - \omega \tau) + 1}{2} \Gamma_0, \quad (63)$$

where D_I is the diffusion in interface tangential direction.

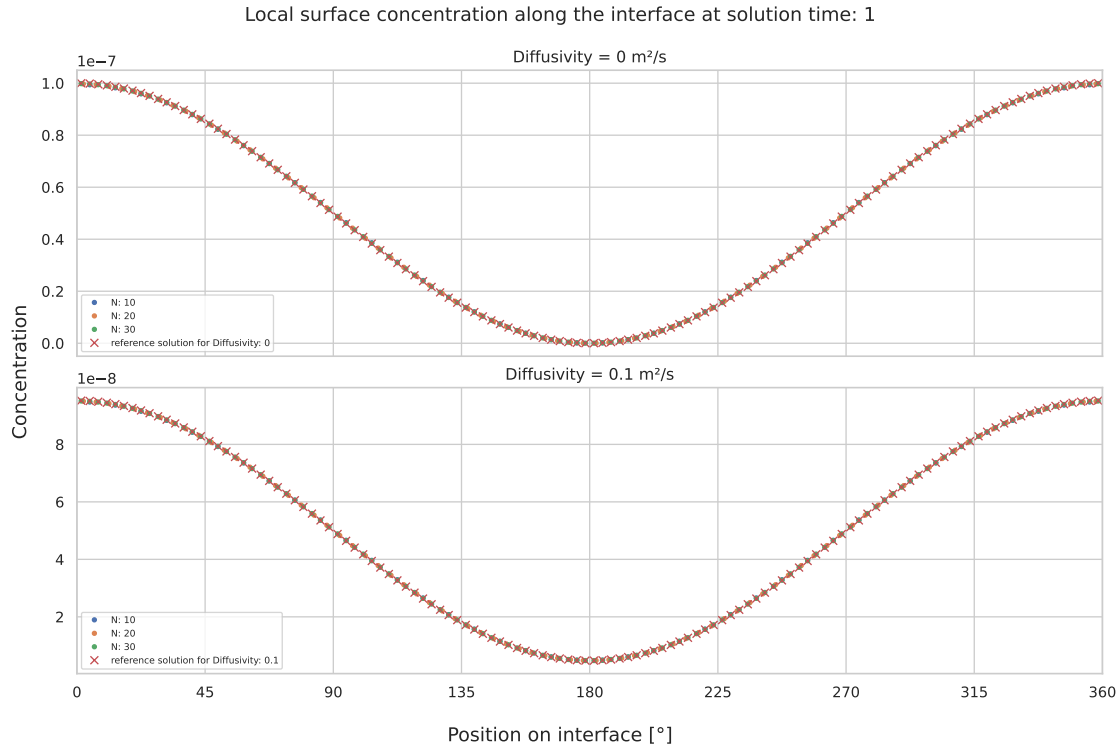


Figure 18: Results from the rotating droplet parameter study

For proper evaluation a mesh refinement study with a parameter variation of the diffusivity is conducted. The results are visualized in fig. 18. We use a meshing parameter $N = [10, 20, 30]$, which correspond to 40, 80 and 160 surface cells along the interface. The timestep is set to 0.0005 s regardless of the mesh size. The surface diffusivity is varied between $0 \text{ m}^2/\text{s}$ and $0.1 \text{ m}^2/\text{s}$.

Visually it is hard to see a difference between the discretizations in fig. 18. In fig. 19 the error norms and their rate of convergence are shown. The infinity norm and L1-norm are close to 1

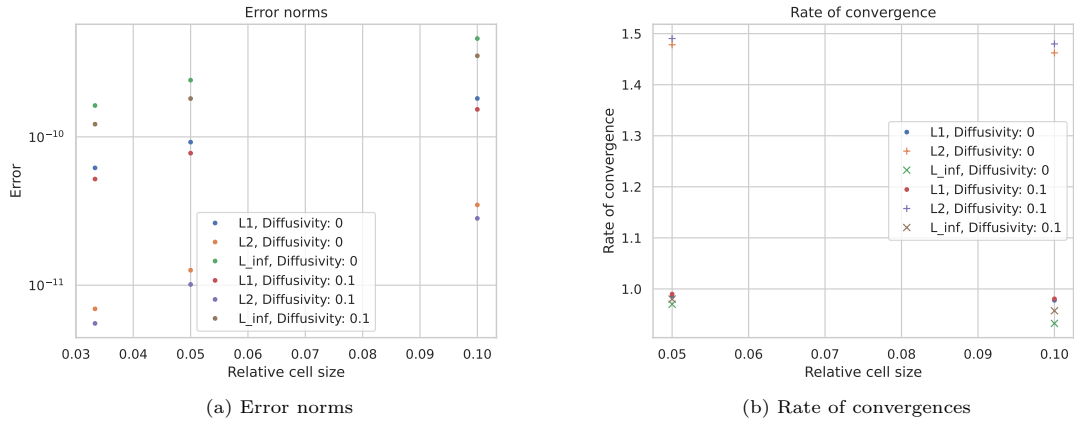


Figure 19: Errors of the rotating droplet parameter study

and the L2-norm is around 1.5 for the resolutions analyzed. With the low error norms and their respective rate of convergence we deduct, that our framework is well able to handle transport along an interface.

6.5. Expanding fluid interface area

To test the frameworks conservation of surfactant mass for an expanding fluid interface area, we implement a test case, that mimics an expanding droplet like it was done by [3, 2]. The initial distribution of species is described and there is no diffusion happening. The initial distribution is the same as in eq. (62). The droplet is represented by a wedge that is inflated with a prescribed velocity and thereby the surface is stretched. The analytical solution to this setup is given by

$$\Gamma(\theta, r(\tau)) = \frac{\cos \theta + 1}{2} \Gamma_0 \frac{r_0^2}{r(\tau)^2}, \quad (64)$$

where $r(\tau) = \sqrt[3]{3V_0(\tau + \tau_0)}$, where $\tau_0 = 1/3s$ and r is the radius, respectively r_0 is the initial radius.

Figure 20 shows, how the species concentration per area at the interface has decreased after 2.5s of bubble growth. The concentration precisely matches the expected result for all mesh resolutions tested. We conclude, that our framework is fit to simulate phenomena involving surface expansion/shrinking.

7. Conclusions

We provide a thoroughly automatically tested implementation of the unstructured Finite-Volume Arbitrary Lagrangian / Eulerian (ALE) Interface-Tracking (IT) method for simulating incompressible, immiscible two-phase flows as an OpenFOAM module.

In conclusion, we have successfully developed a Subgrid-Scale (SGS) model hierarchy within an Arbitrary Lagrangian-Eulerian (ALE) Interface Tracking OpenFOAM module, with configurable

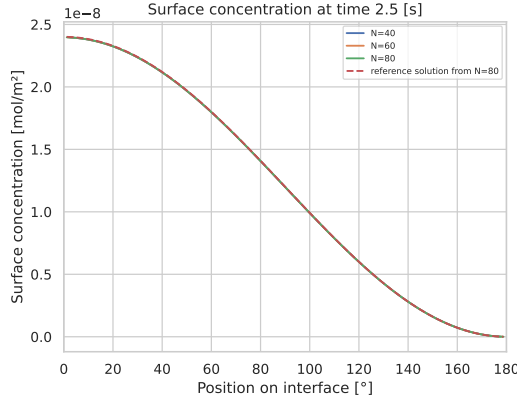


Figure 20: Surface concentration after 0.5 s for different mesh resolutions

output parameters for in-depth analysis. The SGS model's ability to accurately capture thin boundary layers and steep gradients was demonstrated, alongside the critical need for flux correction not only at the interfaces but also across adjacent cell boundaries. Furthermore, the Interface Tracking module's proficiency in accurately simulating surfactants on moving fluid interfaces interfaces and their impact on surface tension and Marangoni flow was demonstrated.

8. Acknowledgments

Moritz Schwarzmeier and Tomislav Marić would like to thank the Federal Government and the Heads of Government of the Länder, as well as the Joint Science Conference (GWK), for their funding and support within the framework of the NFDI4Ing consortium. Funded by the German Research Foundation (DFG) - project number 442146713.

Funded by the German Research Foundation (DFG) – Project-ID 265191195 – SFB 1194.

Part of this work was funded by the Hessian Ministry of Higher Education, Research, Science and the Arts - cluster project Clean Circles.

References

- [1] A. Alke, D. Bothe, M. Kröger, B. Weigand, Dominik Weirich, and H. Weking. Direct numerical simulation of high schmidt number mass transfer from air bubbles rising in liquids using the volume-of-fluid-method. *Ercoftac Bulletin*, 82:5–10, 2010.
- [2] T. Antritter, T. Josyula, T. Marić, D. Bothe, P. Hachmann, B. Buck, T. Gambaryan-Roisman, and P. Stephan. A two-field formulation for surfactant transport within the algebraic volume of fluid method. *Computers & Fluids*, page 106231, March 2024. ISSN 0045-7930. doi: 10.1016/j.compfluid.2024.106231.
- [3] Thomas Antritter. *Numerical Simulation of Coupled Wetting and Transport Phenomena in Inkjet Printing*. PhD thesis, Technische Universität Darmstadt, Darmstadt, 2022. doi: 10.26083/tuprints-00021326.

[4] Dieter Bothe and Stefan Fleckenstein. A volume-of-fluid-based method for mass transfer processes at fluid particles. *Chemical Engineering Science*, 101:283–302, 2013. ISSN 0009-2509. doi: 10.1016/j.ces.2013.05.029.

[5] H. Brenner. *Interfacial Transport Processes and Rheology*. Butterworth-Heinemann series in chemical engineering. Elsevier Science, 2013. ISBN 9781483292274.

[6] K. P. Chen, W. Saric, and H. A. Stone. On the deviatoric normal stress on a slip surface. *Physics of fluids A*, 12(12):3280–3281, 2000.

[7] I. Demirdžić and S. Muzaferija. Numerical method for coupled fluid flow, heat transfer and stress analysis using unstructured moving meshes with cells of arbitrary topology. *Computer methods in applied mechanics and engineering*, 125:235–255, 1995.

[8] I. Demirdžić and M. Perić. Space conservation law in finite volume calculations of fluid flow. *International journal for numerical methods in fluids*, 8:1037–1050, 1988.

[9] Kathrin Dieter-Kissling, Mohsen Karbaschi, Holger Marschall, Aliyar Javadi, Reinhard Miller, and Dieter Bothe. On the applicability of drop profile analysis tensiometry at high flow rates using an interface tracking method. *Colloids and Surfaces A: Physicochemical and Engineering Aspects*, 441:837–845, 2014. doi: 10.1016/j.colsurfa.2012.10.047.

[10] Kathrin Dieter-Kissling, Holger Marschall, and Dieter Bothe. Direct numerical simulation of droplet formation processes under the influence of soluble surfactant mixtures. *Computers & Fluids*, 113:93–105, 2015. doi: 10.1016/j.compfluid.2015.01.017.

[11] J. H. Ferziger and M. Perić. *Computational methods for fluid dynamics*. Springer Verlag, Berlin-New York, 1995.

[12] Mathis Gross, Guillaume Bois, and Adrien Toutant. Thermal boundary layer modelling for heat flux prediction of bubbles at saturation: A priori analysis based on fully-resolved simulations. *International Journal of Heat and Mass Transfer*, 222:124980, May 2024. ISSN 00179310. doi: 10.1016/j.ijheatmasstransfer.2023.124980.

[13] Dirk Gründing, Stefan Fleckenstein, and Dieter Bothe. A subgrid-scale model for reactive concentration boundary layers for 3D mass transfer simulations with deformable fluid interfaces. *International Journal of Heat and Mass Transfer*, 101:476–487, October 2016. ISSN 0017-9310. doi: 10.1016/j.ijheatmasstransfer.2016.04.119.

[14] H. Jasak. *Error analysis and estimation for finite volume method with applications to fluid flows*. PhD thesis, Imperial College, University of London, 1996.

[15] John C. Slattery, Leonard Sagis, and Eun-Suok Oh. *Interfacial Transport Phenomena*. Springer US, Boston, MA, 2007. ISBN 978-0-387-38438-2. doi: 10.1007/978-0-387-38442-9.

[16] Peter A. Kralchevsky, Krassimir D. Danov, and Nikolai D. Denkov. Chemical Physics of Colloid Systems and Interfaces. In K. S. Birdi, editor, *Handbook of Surface and Colloid Chemistry*, page 208. CRC Press, New York, second expanded and updated edition edition, 2002. ISBN 978-0-429-12509-6.

[17] Tomislav Marić, Jens Höpken, and Kyle G. Mooney. *The OpenFOAM technology primer*. March 2021. doi: 10.5281/zenodo.4630596. Version OpenFOAM-v2012.1.

[18] Tomislav Marić, Dennis Gläser, Jan-Patrick Lehr, Ioannis Papagiannidis, Benjamin Lambie, Christian Bischof, and Dieter Bothe. A Research Software Engineering Workflow for Computational Science and Engineering. August 2022. doi: 10.48550/arXiv.2208.07460.

[19] Tomislav Marić, Dennis Gläser, Jan-Patrick Lehr, Ioannis Papagiannidis, Benjamin Lambie, Christian Bischof, and Dieter Bothe. A pragmatic workflow for research software engineering in computational science. 2023. doi: 10.48550/ARXIV.2310.00960.

[20] Metin Muradoglu and Gretar Tryggvason. A front-tracking method for computation of interfacial flows with soluble surfactants. *Journal of Computational Physics*, 227(4):2238–2262, February 2008. doi: 10.1016/j.jcp.2007.10.003.

[21] S. Muzaferija and M. Perić. Computation of free-surface flows using the finite-volume method and moving grids. *Numerical heat transfer, Part B*, 32:369–384, 1997.

[22] Chiara Pesci, Holger Marschall, Talmira Kairaliyeva, Vamsee Krishna Ulaganathan, Reinhard Miller, and Dieter Bothe. Experimental and Computational Analysis of Fluid Interfaces Influenced by Soluble Surfactant. In Dieter Bothe and Arnold Reusken, editors, *Transport Processes at Fluidic Interfaces*, pages 395–444. Springer International Publishing, Cham, 2017. ISBN 978-3-319-56602-3. doi: 10.1007/978-3-319-56602-3_15.

[23] Chiara Pesci, Andre Weiner, Holger Marschall, and Dieter Bothe. Computational analysis of single rising bubbles influenced by soluble surfactant. *Journal of Fluid Mechanics*, 856:709–763, 2018. ISSN 0022-1120, 1469-7645. doi: 10.1017/jfm.2018.723.

[24] R. Satapathy and W. Smith. The motion of single immiscible drops through a liquid. *Journal of Fluid Mechanics*, 10(4):561, 1961. ISSN 0022-1120, 1469-7645. doi: 10.1017/S0022112061000366.

[25] M. Schwarzmeier, S. Raju, Z. Tuković, and T. Marić. Twophaseintertrackfoam source code repository. GitLab, 2024. URL https://gitlab.com/interface-tracking/twophaseintertrackfoamrelease/-/tree/v1.0?ref_type=tags. Accessed: 2024-03-24.

[26] Moritz Schwarzmeier, Suraj Raju, Zeljko Tuković, and Tomislav Marić. twophaseintertrackfoam - data & results v1.0, 2024-03-24.

[27] P. D. Thomas and C. K. Lombard. Geometric conservation law and its application to flow computations on moving grids. *AIAA Journal*, 17:1030–1037, 1979.

[28] Željko Tuković and Hrvoje Jasak. Simulation of free-rising bubble with soluble surfactant using moving mesh finite volume/area method. In *Proceedings of 6th International Conference on CFD in Oil & Gas, Metallurgical and Process Industries*, no. CFD08-072, 2008.

[29] Željko Tuković, Milovan Perić, and Hrvoje Jasak. Consistent second-order time-accurate non-iterative PISO-algorithm. *Computers & Fluids*, 166:78–85, April 2018. doi: 10.1016/j.compfluid.2018.01.041.

- [30] Zeljko Tuković, Moritz Schwarzmeier, Suraj Raju, and Tomislav Marić. twophaseintertrack-foam - code, 2024-03-24. doi: 10.48328/tudatalib-1395.
- [31] Željko Tuković and Hrvoje Jasak. A moving mesh finite volume interface tracking method for surface tension dominated interfacial fluid flow. *Computers & Fluids*, 55:70–84, February 2012. doi: 10.1016/j.compfluid.2011.11.003.
- [32] C. E. Weatherburn. *Differential geometry in three dimension*. Cambridge University Press, London, 1972.
- [33] Paul S Weber, Holger Marschall, and Dieter Bothe. Highly accurate two-phase species transfer based on ale interface tracking. *International Journal of Heat and Mass Transfer*, 104:759–773, 2017.
- [34] Andre Weiner and Dieter Bothe. Advanced subgrid-scale modeling for convection-dominated species transport at fluid interfaces with application to mass transfer from rising bubbles. *Journal of Computational Physics*, 347:261–289, 2017. ISSN 00219991. doi: 10.1016/j.jcp.2017.06.040.
- [35] Andre Weiner, Dirk Gründing, and Dieter Bothe. Computing Mass Transfer at Deformable Bubbles for High Schmidt Numbers. *Chemie Ingenieur Technik*, 93(1-2):81–90, 2021. ISSN 1522-2640. doi: 10.1002/cite.202000214.
- [36] N. O. Young, J. S. Goldstein, and M. J. Block. The motion of bubbles in a vertical temperature gradient. *Journal of Fluid Mechanics*, 6(03):350, October 1959. doi: 10.1017/s0022112059000684.